

Radiative properties and direct radiative effect of Saharan dust measured by the C-130 aircraft during SHADE:

1. Solar spectrum

Jim Haywood,¹ Pete Francis,¹ Simon Osborne,¹ Martin Glew,¹ Norman Loeb,² Eleanor Highwood,³ Didier Tanré,⁴ Gunnar Myhre,⁵ Paola Formenti,^{6,7} and Edwin Hirst⁸

Received 21 June 2002; revised 17 September 2002; accepted 22 November 2002; published 18 July 2003.

[1] The physical and optical properties of Saharan dust aerosol measured by the Met Office C-130 during the Saharan Dust Experiment (SHADE) are presented. Additional radiation measurements enable the determination of the aerosol optical depth, $\tau_{aer,\lambda}$, and the direct radiative effect (DRE) of the mineral dust. The results suggest that the absorption by Saharan dust is significantly overestimated in the solar spectrum if standard refractive indices are used. Our measurements suggest an imaginary part of the refractive index of $0.0015i$ is appropriate at a wavelength λ of $0.55 \mu\text{m}$. Different methods for determining $\tau_{aer,\lambda=0.55}$ are presented, and the accuracy of each retrieval method is assessed. The value $\tau_{aer,\lambda=0.55}$ is estimated as 1.48 ± 0.05 during the period of heaviest dust loading, which is derived from an instantaneous DRE of approximately $-129 \pm 5 \text{ Wm}^{-2}$ or an enhancement of the local planetary albedo over ocean of a factor of 2.7 ± 0.1 . A comparison of the DRE derived from the C-130 instrumentation and from the Clouds and the Earth's Radiant Energy System (CERES) instrument on the Tropical Rainfall Measuring Mission (TRMM) satellite is presented; the results generally showing agreement to within a factor of 1.2. The results suggest that Saharan dust aerosol exerts the largest local and global DRE of all aerosol species and should be considered explicitly in global radiation budget studies.

INDEX TERMS: 0305 Atmospheric Composition and Structure: Aerosols and particles (0345, 4801); 0360 Atmospheric Composition and Structure: Transmission and scattering of radiation; 1640 Global Change: Remote sensing; 3359 Meteorology and Atmospheric Dynamics: Radiative processes;
KEYWORDS: aerosols, Saharan dust, radiative forcing, radiation balance, mineral dust, aircraft measurements

Citation: Haywood, J., P. Francis, S. Osborne, M. Glew, N. Loeb, E. Highwood, D. Tanré, G. Myhre, P. Formenti, and E. Hirst, Radiative properties and direct radiative effect of Saharan dust measured by the C-130 aircraft during SHADE: 1. Solar spectrum, *J. Geophys. Res.*, 108(D18), 8577, doi:10.1029/2002JD002687, 2003.

1. Introduction

[2] The radiative effects of mineral dust aerosol have received an increasing amount of attention in recent years [Sokolik *et al.*, 2001, and references therein]. Saharan dust aerosol is of particular interest as locally it exerts the strongest perturbation to the top of the atmosphere solar radiation budget of all aerosol species by scattering radiation back to space [e.g. Haywood *et al.*, 1999]. In addition Saharan dust may exert a significant perturbation to the

terrestrial radiation owing to the large size of the aerosol particles as evidenced by the modeling studies of Myhre and Stordal [2001] and Woodward [2001]. A significant amount of Saharan dust may be generated by anthropogenic activities such as over-grazing in the Sahel [e.g. Tegen and Fung, 1995], and therefore mineral dust may exert a significant radiative forcing, i.e. the anthropogenic component of the radiative effect. Because of the complexities of the competing solar and terrestrial radiative forcings, even the sign of the radiative forcing is unknown. Intergovernmental Panel on Climate Change [2001] suggests a radiative forcing in the range $+0.4 \text{ Wm}^{-2}$ to -0.6 Wm^{-2} , which may be significant when compared to a radiative forcing due to increases in well-mixed greenhouse gases of $+2.45 \text{ Wm}^{-2}$.

[3] Haywood *et al.* [2001a] used instruments on the C-130 aircraft to measure an instantaneous perturbation to the top of the atmosphere reflected solar radiation field as strong as -60 Wm^{-2} . Haywood *et al.* [2001b] investigated the consistency of the aerosol optical depth, $\tau_{aer,\lambda}$, derived from the aircraft measurements with the 2-channel aerosol retrieval from the Advanced Very High Resolution Radiometer (AVHRR), finding good agreement. Both of these studies were performed on essentially an opportunist basis while the

¹Met Office, Bracknell, UK.

²NASA Langley Research Center, Hampton, Virginia, USA.

³Department of Meteorology, Reading University, Reading, UK.

⁴Laboratoire d'Optique Atmosphérique, Centre Nationale de Recherche Scientifique, Université de Sciences et Techniques de Lille, Lille, France.

⁵Department of Geophysics, University of Oslo, Oslo, Norway.

⁶Max Planck Institute for Chemistry, Mainz, Germany.

⁷Now at Laboratoire Interuniversitaire des Systèmes Atmosphériques, Faculté des Sciences et Technologie,

⁸Science and Technology Research Centre, University of Hertfordshire, Hatfield, UK.

C-130 aircraft was on route between Tenerife and Ascension Island.

[4] This study provides a more thorough investigation while the C-130 aircraft was operating from Sal, Cape Verde Islands in the period 19–28 September 2000, during the Saharan Dust Experiment (SHADE). The study presents an analysis of the physical and optical properties of Saharan dust collected from all of the flights, and then concentrates on determining the solar direct radiative effect and optical depths during a strong dust event on 25 September 2000. *Highwood et al.* [2003] provide complementary C-130 measurements of the magnitude and spectral dependence of the terrestrial radiative effects of Saharan dust. *Tanré et al.* [2003] provide a summary of the flight patterns and operating procedures of the C-130 aircraft, and those of the Mystere aircraft that was operating concurrently.

[5] The instrumentation of the C-130 is discussed in section 2, and section 3 presents a summary of the flight patterns and meteorological conditions. Aerosol size distributions obtained from the PCASP-100X instrument are presented in section 4 and measured and modeled optical parameters are presented in section 5. Section 6 presents different methods of obtaining the aerosol optical depth, $\tau_{aer\lambda}$ which is compared against surface observations in section 7. Section 8 presents estimates of the aerosol direct radiative effect, DRE, from the aircraft measurements, and from the Cloud's and Earth's Radiant Energy Systems (CERES) satellite instrument, before a discussion and conclusions in section 9.

2. Relevant Instrumentation

[6] The aerosol and radiation instrumentation used in this measurement campaign is identical to that used in the Southern African Regional Science Initiative (SAFARI 2000) described by *Haywood et al.* [2003a, 2003b]. Briefly, aerosol chemistry was determined from isokinetic sampling onto filter substrates. Two filter packs were used: quartz filter packs for apparent elemental black carbon (EC_a) and organic carbon (OC) analysis, and Teflon packs for major cation and anion chromatography. These packs had Nuclepore filters mounted in front of them to fractionate the particles into a coarse (onto the Nuclepore) and fine (onto the Teflon or quartz) fraction, the approximate cut between coarse and fine particles being $0.5 \mu\text{m}$ aerodynamic radius. The quartz filters were subsequently analyzed for EC_a and OC, while the Teflon and Nuclepore filters were analyzed for water-soluble ions and inorganic elemental components [*Formenti et al.*, 2003].

[7] Particulate absorption of radiation of wavelength $0.567 \mu\text{m}$ was measured with a Radiance Research Particle Soot Absorption Photometer (PSAP). Aerosol scattering was determined at 3 wavelengths (0.45 , 0.55 , $0.70 \mu\text{m}$) with a TSI 3563 nephelometer. Carbon monoxide measurements (resonance-fluorescence technique, developed by fz-Juelich) were made throughout the SHADE campaign.

[8] Aerosol size distributions between 0.05 and $1.5 \mu\text{m}$ radius were determined with a Particle Measuring System (PMS) Passive Cavity Aerosol Spectrometer Probe 100X (PCASP). A Fast Forward Scattering Spectrometer Probe (FFSSP) developed from a PMS FSSP was used to measure aerosol and cloud particles between 1 and $23.5 \mu\text{m}$ radius.

As noted by *Haywood et al.* [2003a], the FFSSP did not operate correctly throughout SAFARI 2000, and the same problems occurred in SHADE. The Small Ice Detector (SID) [*Hirst et al.*, 2001] was also fitted. SID was originally designed to measure particle shape, size and concentration for discrimination between supercooled water drops and ice crystals in the radius range 0.5 – $12 \mu\text{m}$, however, aerosol particles are also detectable.

[9] The following radiation equipment was fitted to the C-130. Upward and downward facing Eppley broadband radiometers (BBRs) were fitted with clear and red domes covering the 0.3 – $3.0 \mu\text{m}$ and 0.7 – $3.0 \mu\text{m}$ spectral regions respectively each with an aft mounted obscurer [*Foot*, 1986; *Hignett et al.*, 1999; *Haywood et al.*, 2001a, 2001b]. The Met Office Scanning Airborne Filter Radiometer (SAFIRE) was designed to measure radiances in 16 bands across the visible and near-infrared region of the spectrum and was mounted in a pod on the port wing of the C-130 [*Francis et al.*, 1999]. During the detachment, only seven of the channels were operated providing radiances at 0.55 , 0.62 , 0.87 , 1.04 , 1.25 , 1.61 , and $2.01 \mu\text{m}$. An additional instrument installed on the C-130 is the short-wave spectrometer (SWS) which uses 2 Carl Zeiss spectrometer modules operating in the spectral range 0.30 – $0.95 \mu\text{m}$ and 0.95 – $1.70 \mu\text{m}$. These are connected via optic fibers to a simple light gathering telescope (half angle 0.75°) viewing through a downward pointing aperture thereby providing a nadir view. The pixel separation is approximately $0.0033 \mu\text{m}$ in the 0.30 – $0.95 \mu\text{m}$ module and $0.006 \mu\text{m}$ in the 0.95 – $1.70 \mu\text{m}$ module, giving approximate spectral resolutions of $0.010 \mu\text{m}$ and $0.018 \mu\text{m}$ respectively.

3. Flight Patterns and Meteorological Conditions

[10] The aircraft performed four dedicated flights from Sal, Cape Verde Islands on 21, 24, 25, and 28 September 2000. Aircraft sampling of aerosol physical and optical properties was also performed during profiles into/out of Sal on three other occasions on 23 and 31 August 2000 and on 19 September 2000. *Tanré et al.* [2003] provides the flight tracks of the C-130 and the Mystere aircraft during the campaign. During the period of intensive investigation, very little dust aerosol was encountered on 21 September, moderate aerosol concentrations were sampled on 24 September, and heavy aerosol concentrations were sampled on 25 September as a large Saharan dust storm was advected westward over the operating region [*Tanré et al.*, 2003]. The C-130 aircraft became unserviceable subsequent to the flight on 25 September and was not operational again until 28 September 2000 where moderate concentrations of aerosol were experienced. Table 1 summarizes the flight numbers and dates of the flights.

[11] While the transit flights concentrated on in situ sampling of aerosol physical properties, the dedicated flights consisted of straight and level runs (SLRs) above (maximum altitude $\sim 6 \text{ km}$), within and below the aerosol layers to enable determination of the radiative effect and optical depth of the aerosol [*Hignett et al.*, 1999; *Haywood et al.*, 2001a, 2001b].

[12] The flight pattern flown during flight a797 on 25 September 2000 during the large dust event, is shown schematically in Figure 1. During this flight a large dust

Table 1. Description of Flights and $\omega_{0\lambda}$ Derived From the PSAP and Nephelometer Which Applies the Corrections to Absorption Described by *Bond et al.* [1999] and the Corrections to Scattering Described by *Anderson and Ogren* [1998]^a

Flight Number, Date	Comment	$\omega_0 \pm 0.02$		
		$\lambda = 0.45$	$\lambda = 0.55$	$\lambda = 0.70$
A778, 23 Aug.	transit from UK	*	*	*
A783, 31 Aug.	transit to Ascension Island	*	*	*
A794, 19 Sept.	transit from Ascension Island	0.99	0.99	1.00
A795, 21 Sept.	dedicated flight	0.95	0.96	0.97
A796, 24 Sept.	dedicated flight	0.96	0.97	0.97
A797, 25 Sept.	dedicated flight	0.94	0.95	0.95
A798, 28 Sept.	dedicated flight	0.98	0.98	0.99
Mean		0.96	0.97	0.98

^a $\omega_{0\lambda = 0.55}$ are indicated by boldface. The effects of relative humidity are considered negligible. The asterisks indicate where data are unavailable.

storm was advected off the coast of WEST Africa toward the Cape Verde Islands. The SLRs were typically of more than 10 min duration and profiles were flown in-between to determine the vertical extent of the dust. Additionally, orbits were performed below the dust layer to determine the angular distribution of the radiances from SAFIRE [Francis *et al.*, 1999].

[13] Dropsondes were deployed during flight a797 (Figure 1) to determine atmospheric temperature, humidity and wind speed and direction. Tephigrams showing the temperature and humidity below the C-130 during R6 are shown in Figure 2, the most westerly profile being presented in Figure 2a, and the most easterly profile being presented in Figure 2d. Three distinct layers can be seen in each of the tephigrams:

[14] 1. Approximately 1020–950 hPa: Marine boundary layer (MBL). The relative humidity was typically 80–90%,

and was separated from the overlying dust layer by a temperature inversion of approximately 5 K.

[15] 2. Approximately 950–600 hPa: Dust layer. This layer was the remnants of the continental boundary layer and contained Saharan dust that had been advected off the coast of WEST Africa by the easterly winds associated with the African easterly jet. The water vapor mixing ratios were typically 3–8 g kg⁻¹ and the relative humidity ranged from approximately 30% at 950 hPa to 70% at 600 hPa. The presence of dust in this layer is confirmed by looking at the asphericity factor from the SID probe which has also been used to look at aerosol predominated by biomass burning aerosol [Haywood *et al.*, 2003a]. In Figure 3, values above unity are indicative of nonspherical scattering patterns while those below unity suggest scattering by particles that are spherical in nature.

[16] 3. Approximately 600 hPa upward: Free troposphere. Dry, aerosol-free layer with relative humidities of typically 10–20%.

[17] The tephigrams presented in the studies of Saharan dust by *Karyampudi et al.* [1999], and *Haywood et al.* [2001a] show many similarities to those presented here.

4. Aerosol Size Distributions Measured During SHADE

[18] Aerosol size distributions were available from the PCASP for the duration of the campaign. No adjustment of the PCASP measured size distribution accounting for the differing refractive index of mineral dust and the PCASP-100X calibrating spheres was applied. This is because the refractive index of latex at the PCASP-100X laser wavelength of 0.635 μm is approximately $1.58 + 0i$, while the corresponding refractive index of mineral dust is $1.53 + 0.008i$ according to *WCP* [1986], and $1.56 + 0.006i$ accord-

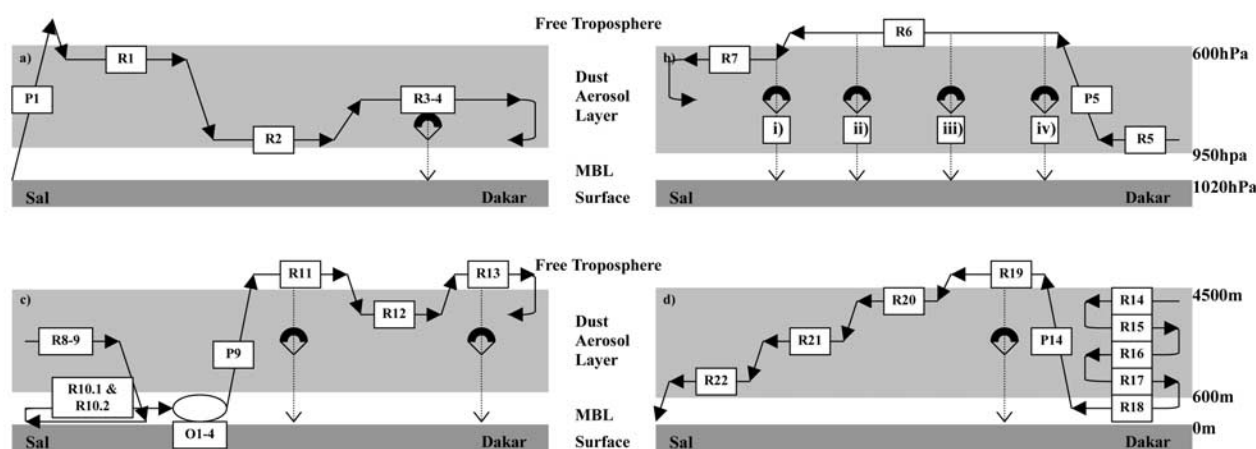


Figure 1. Sequence of the flight patterns flown on flight a797 on the 25 September 2000 between Sal, Cape Verde Islands (left-hand side of the figures) and Dakar (right-hand side of the figures), Senegal. “R” indicates a straight and level run (SLR), “P” indicates profile, and “O” indicates orbit. Only a limited number of major profiles are numbered in the diagram. The approximate position of the dropsondes is also shown by the vertical dotted arrows and the parachutes. The times of the flight patterns were (a) 10:00–11:55 UTC, (b) 11:58–13:37 UTC, (c) 13:42–16:06 UTC, and (d) 16:12–18:45 UTC. The approximate altitudes (m ASL) and pressures (hPa) of the surface and top of the MBL and aerosol layer are also shown. Tephigrams from the dropsondes i–iv are shown in Figure 2. The Sun photometer site are at approximately 22.93°W for Sal Island and at 16.95°W for Dakar.

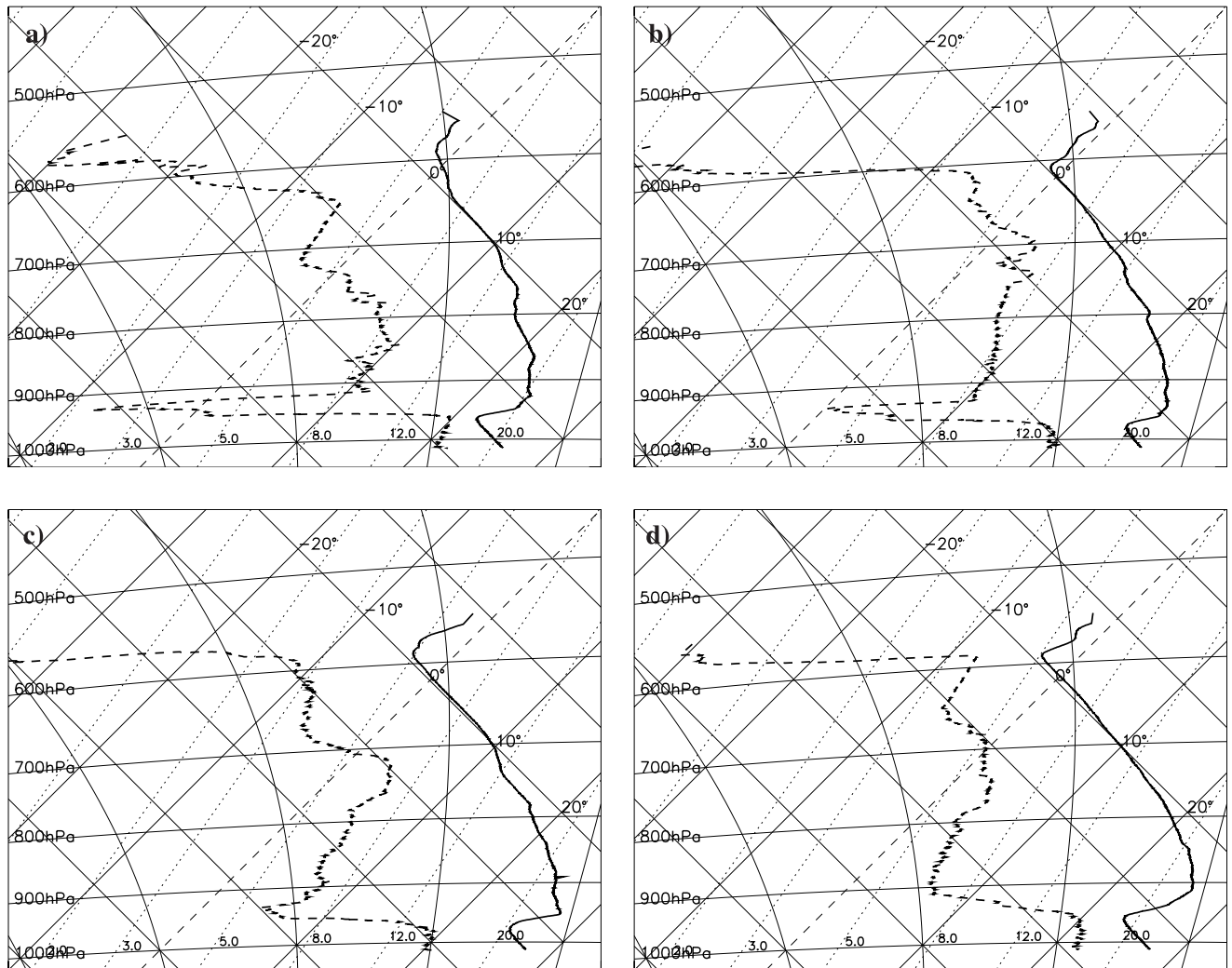


Figure 2. Tephigrams showing the atmospheric profile of temperature and humidity from dropsondes during R6 of flight a797. Figure 2a shows the most westerly profile closest to Sal, and Figure 2d shows the most easterly profile closest to Dakar, the approximate relative positions being marked on Figure 1b. The launch longitudes of the sondes were (a) 22.63°W , (b) 21.21°W , (c) 19.84°W , and (d) 18.46°W .

ing to *Patterson et al.* [1977] and is thus broadly similar. As we shall see in section 5, the absorption by mineral dust using these values of the imaginary refractive index appears overestimated and a value of 0.0015i appears more appropriate. A correction for nonsphericity of the particles is difficult to account for without knowledge of the morphology of the particles, and detailed scattering calculations, and so the assumption of spherical particles is made here. The mean aerosol size distribution ($dn/d\ln r$) encountered during SLRs in the mineral dust layers for each flight is shown in Figure 4. Generally, the aerosol size distributions fall into two groups. The flights a796, a797, and a798 all show similar size distribution characteristics while the size distributions from flights a778, a783, and a794 show significantly fewer large particles. The vertical bars on Figure 4 represent the standard deviations of the size distributions computed from the individual SLRs that make up the flight average size distributions for a794 and a797. While it is possible that fewer particles may be indicative of longer range transport it could also be differences in source area

that lead to these different size distributions. The modeling study of *Myhre et al.* [2003] suggests that the source of the main dust storm during flights a796, a797, and a798 are the western or central Sahara. However, the detailed assessment of the evolution of the dust size distribution is beyond the scope of the study presented here. Two aerosol size distributions are used in this study corresponding to the mean for a796, a797, and a798, and the mean for a778, a783, and a794. These two size distributions are henceforth called Dust A, and Dust B cases.

[19] The mean aerosol number distributions for Dust A and Dust B are fitted with five lognormal size distributions as shown in Figure 5. The lognormal distributions have the form:-

$$\frac{dn_i(r)}{d\ln r} = \frac{n_i}{\sqrt{2\pi} \ln \sigma} \exp \left[-\frac{(\ln r_i - \ln r_n)^2}{2(\ln \sigma)^2} \right], \quad (1)$$

where $dn_i(r)$ is the number of particles in the range $\ln r$ to $\ln r + d\ln r$, and r_n and σ are the geometric mean radii and

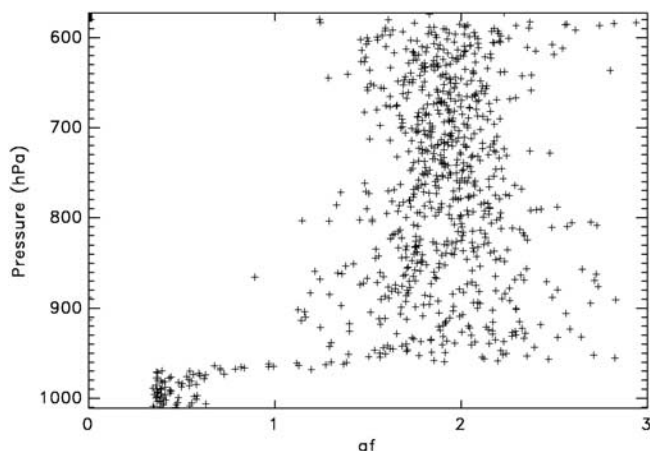


Figure 3. The asphericity factor af of particles in the radius range $0.5\text{--}12\ \mu\text{m}$ detected by the Small Ice Detector (SID) during profile P9 of flight a797. Values greater than unity (950–580 hPa) suggest nonspherical scattering patterns, while those less than unity (1010–950 hPa and <580 hPa) suggest spherical scattering patterns.

standard deviations. Table 1 suggests that r_n and σ do not vary significantly between the Dust A and Dust B cases, but the contribution to the total number of mode 3 and mode 4 increases in the Dust A case. Mode 5 is poorly constrained by the PCASP measurements which detects particles with radii up to approximately $1.5\ \mu\text{m}$. However, this mode may be important in determining the influence of mineral dust in both the solar spectrum and the terrestrial regions of the spectrum [e.g. *Highwood et al.*, 2003]. These sizes are also of interest to modeling efforts [e.g. *Myhre et al.*, 2003] as this mode contains a significant fraction of the aerosol mass. In deriving the largest mode, the Sun photometer size distributions derived from the retrieval algorithms of *Nakajima et al.* [1996], and *Dubovik and King* [2000] are used. These size distributions are retrieved from surface-based Sun photometers sited in Sal and Dakar on 25 September 2000 (corresponding to flight a797). No Sun photometer derived size distributions from Sal or Dakar are available for any of the flights where the Dust B size distribution was measured and therefore the simple assumption that mode 5 does not vary between Dust A and Dust B size distributions is made. While the validity of this assumption is questionable, it should be noted that the radiative transfer calculations in sections 6–8 all use the Dust A distribution.

[20] Sun photometer retrieval algorithms use measurements of the angular distribution of the sky radiance and radiative transfer modeling to determine the aerosol size distributions averaged over the atmospheric column. The largest lognormal mode (mode 5) in the Dust A distribution is fitted by eye to those shown in Figure 6. Figure 6 shows the Sun photometer derived size distributions consisting of means from 25 September 2000 (13 measurement for *Nakajima et al.* [1996], and 6 from *Dubovik and King* [2000] from the sites at Sal and Dakar) together with the Dust A model plotted as $dV/d\ln r$. The double peak in the PCASP volume distributions is evident in many of the individual retrievals of both the *Dubovik and King* [2000]

and *Nakajima et al.* [1996] algorithms, but disappears when the temporal averaging is performed [see also *Highwood et al.*, 2003]. Also note that the increase in the volume of the particles at radii less than approximately $0.1\ \mu\text{m}$ in the *Dubovik and King* [2000] retrievals is an artifact caused by the effects of nonsphericity of the aerosol. This artifact has been corrected for in more recent retrieval algorithms by modeling the aerosol particles as a mixture of prolate and oblate spheroids [*Dubovik et al.*, 2002].

[21] In performing the fit to the Sun photometer size distributions, the Dust A size distribution has to be normalized by an appropriate factor because the aircraft measurements measure volume size distributions per unit volume of sampled air, whereas the Sun photometer measurements determine the mean column integrated volume size distribution. *Haywood et al.* [2003b] showed that the size distributions derived from Sun photometers and measured by the PCASP-100X instrument were very similar for well-mixed biomass burning aerosol. In using the Sun photometer size distributions to deduce the largest mode, it is assumed that they are representative of mineral dust and are not contaminated by other aerosol size distributions such as sea salt. This is likely to be a reasonable assumption as it will be shown the optical depth of the mineral dust aerosol is high in this case (section 6). These calculations also assume that the Sun photometer retrievals are not affected by the effects of nonsphericity of the particles which should be a reasonable assumption for the supermicron particles but may introduce artifacts for particles of less than approximately $0.1\ \mu\text{m}$ radius [e.g. *Dubovik et al.*, 2002].

5. Aerosol Optical Properties

[22] The chemical composition of the aerosol is discussed in detail by *Formenti et al.* [2003], and is not discussed in detail here. In our calculations of the optical properties of mineral dust aerosol, two different methods are used to determine the aerosol optical properties. First, measure-

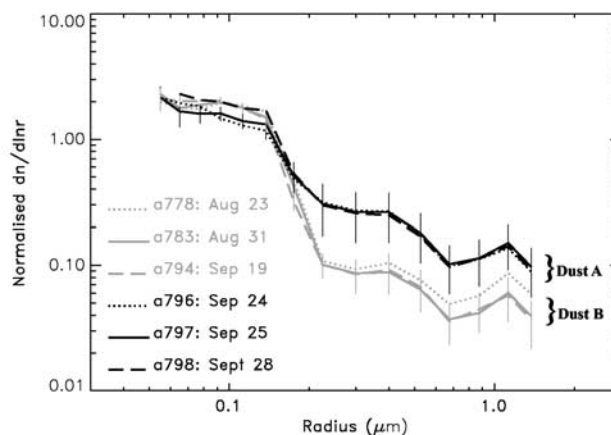


Figure 4. The aerosol size distributions collected from SLRs within the mineral dust layer plotted as normalized $dn/d\ln r$ for each of the flights performed during SHADE. The Dust A and Dust B groupings are shown. The vertical bars represent the standard deviation of the size distributions between the different SLRs that make up the flight averaged size distribution and are shown for flights a797 and a794.

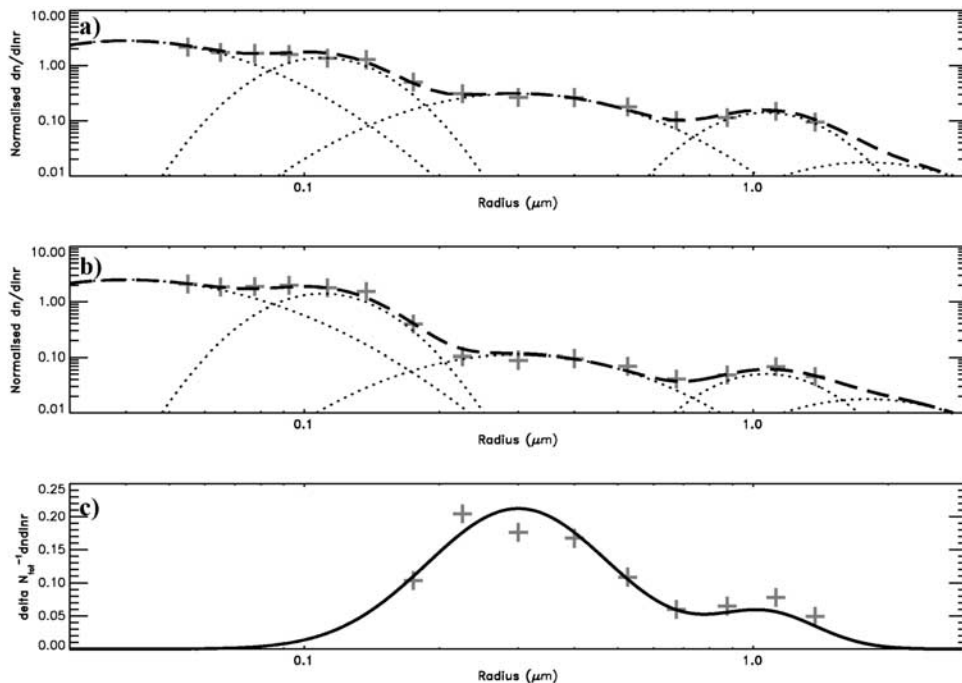


Figure 5. The five lognormal distributions used in fitting the aerosol size distributions shown in Figure 4. (a) The size distribution Dust A from the mean of the size distributions measured in a796, a797, and a798. (b) The size distribution Dust B from the mean of the size distributions measured in a778, a783, and a794. (c) The difference in normalized aerosol size distributions (+) and the difference in the sum of mode 3 and mode 4 lognormal fits.

ments with the PSAP and nephelometer are used to determine the single scattering albedo at wavelength, λ , $\omega_{o\lambda=0.55}$. The second set of calculations use the measured size distribution in conjunction with appropriate refractive indices and densities to determine $\omega_{o\lambda}$, the asymmetry factor, g_{λ} , and the specific extinction coefficient, $k_{e\lambda}$.

5.1. Determination of $\omega_{o\lambda}$ From In Situ Nephelometer and PSAP Data

[23] Measurements were performed using the PSAP and nephelometer over periods identical to those used in calculating the PMS mean aerosol size distributions shown in Figure 4. The Rosemount inlet collection efficiency drops from close to unity to close to zero for particle radii greater than 1–2 μm , so the nephelometer and PSAP measurements apply to submicron aerosol particles. The nephelometer was corrected for variations from STP, for truncation of the forward-scattered radiation, and for deficiencies in the illumination source [Anderson and Ogren, 1998]. The PSAP was corrected for variations in the area of the exposed filter, inaccuracies in the flow rate measured by the instrument, for scattering being misinterpreted as absorption, and for multiple scattering [Bond et al., 1999]. Both of these sets of corrections tend to decrease the absorption coefficient while increasing the scattering coefficient hence raising ω_o [see Haywood and Osborne, 2000]. While the nephelometer measures at three wavelengths (0.45, 0.55, and 0.70 μm), the PSAP measures the absorption at 0.567 μm . This enables determination of $\omega_{o\lambda=0.55}$ to a reasonable accuracy, but assumptions have to be made about the wavelength dependence of the absorption coefficient to enable estimation of $\omega_{o\lambda=0.45}$ and $\omega_{o\lambda=0.70}$. Here we make the reasonable assump-

tion that the absorption coefficient is proportional to $1/\lambda$. The model calculations suggest this is a more realistic assumption than a wavelength independent absorption coefficient. The results are summarized in Table 1, which shows $\omega_{o\lambda=0.55}$ ranging from 0.95 ± 0.02 to 0.99 ± 0.02 with a mean of 0.97 ± 0.02 . The error estimate of $\omega_{o\lambda=0.55}$ of ± 0.02 follows the analysis of Haywood and Osborne [2000]

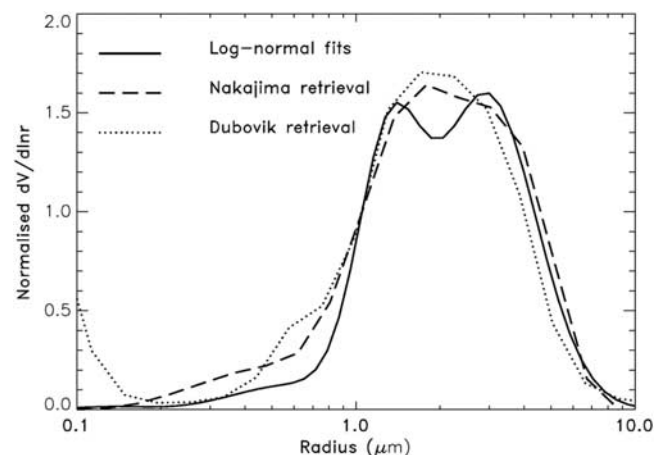


Figure 6. Comparison of the size distributions ($dV/d\ln r$) derived from the lognormal fits (solid line) and those derived from the Nakajima et al. [1996] retrieval and the Dubovik and King [2000] retrieval. All measurements are normalized to equal 1 at 1.0 μm . The apparent large increase in the volume concentration at 0.1 μm radius in the Dubovik retrievals is an artefact caused by the influence of nonspherical particles [see Dubovik et al., 2002].

Table 2. Geometric Mean Radii r_n and Standard Deviations σ for Each of the Lognormal Modes of the Aerosol Number Distributions Shown in Figure 5^a

	n_i Dust A	n_i Dust B	r_n , μm	σ	$k_{e\lambda=0.55}$, m^2g^{-1}	$\omega_{o\lambda=0.55}$	$g_{\lambda=0.55}$	Percent Contribution to $\tau_{aer\lambda=0.55}$, Dust A	Percent Contribution to $\tau_{aer\lambda=0.55}$, Dust B
Mode 1	0.703	0.750	0.04	1.6	0.89	0.98	0.41	0.2	0.5
Mode 2	0.195	0.208	0.11	1.3	2.11	0.99	0.55	8.9	3.2
Mode 3	0.077	0.030	0.30	1.6	1.64	0.98	0.67	20.4	14.5
Mode 4	0.020	0.007	1.07	1.3	0.53	0.94	0.75	39.3	25.0
Mode 5	0.005	0.005	1.8	1.5	0.23	0.90	0.80	31.2	56.8
Dust A	*	*	*	*	0.42	0.95	0.74	*	*
Dust A Excluding Mode 5	*	*	*	*	0.70	0.95	0.72	*	*
Dust B	*	*	*	*	0.33	0.92	0.76	*	*
Dust B Excluding Mode 5	*	*	*	*	0.74	0.96	0.70	*	*

^aThe optical parameters for the Dust A and Dust B size distributions are also shown excluding mode 5. Asterisks indicate where the parameters are not applicable.

for Saharan dust aerosol. While the relative error in $\omega_{o\lambda=0.55}$ is small at 2%, it is the coalbedo ($1 - \omega_{o\lambda=0.55}$) that determines the absorption, and the relative error in the coalbedo is up to approximately 70% indicating that the uncertainty in the absorption is significant.

5.2. Determination of Optical Properties From In Situ Size Distribution Measurements With the PCASP

[24] The optical properties of the dust size distributions Dust A and Dust B are calculated using Mie scattering theory. These calculations make the assumption that at $\lambda = 0.55 \mu\text{m}$ the real part of the refractive index, $re_{\lambda=0.55}$, for dust is 1.53 and follows the wavelength dependence of the dust-like particles of *World Climate Program (WCP)* [1986]. *Sokolik and Toon* [1996] present a summary of many different measurements of re_{λ} and indicate this value should be reasonable. The imaginary part of the refractive index at $\lambda = 0.55 \mu\text{m}$, $im_{\lambda=0.55}$, is more difficult to determine as *Sokolik and Toon* [1996] show variations over 3 orders of magnitude for different mineral dust components. *WCP* [1986] suggest $im_{\lambda=0.55}$ of $0.008i$ in the wavelength range 0.3–2.0 μm . More recently, aerosol data sets such as the Optical Properties of Aerosols and Clouds (OPAC) developed by *Hess et al.* [1998] reduce the absorption by a factor of two in some of this spectral region. *Kaufman et al.* [2001] used remote sensing to infer that the absorption by Saharan dust is even less and suggest an $\omega_{o\lambda=0.55}$ of 0.97. *Clarke et al.* [2001] made aircraft observations of dust transported from Asia using very similar instrumentation to that used here, and found that an $\omega_{o\lambda=0.55}$ of 0.97 was representative of pure mineral dust.

[25] Our calculations assume a real and imaginary refractive index based on *WCP* [1986] except for adjustment of im_{λ} from $0.008i$ to $0.0015i$ in the wavelength range 0.3–2.0 μm . This $0.0015i$ refractive index leads to an $\omega_{o\lambda=0.55}$ of 0.95 for Dust A when either 4 or 5 five modes are used to model the size distribution. When comparing $\omega_{o\lambda=0.55}$ from this method against those derived from the PSAP and nephelometer, only 4 modes should be included in the PCASP-based calculations because of the cutoff of the Rosemount inlet between 1 and 2 μm radius. $\omega_{o\lambda=0.55}$ of 0.95 and 0.96 for Dust A and Dust B is in reasonable agreement with $\omega_{o\lambda=0.55}$ derived from measurements by the PSAP and nephelometer (Tables 1 and 2). If $im_{\lambda=0.55} = 0.008i$ is used in the calculations and mode 5 is

excluded, then $\omega_{o\lambda=0.55}$ of 0.86 occurs for both Dust A and Dust B which is inconsistent with the measurements presented in section 5.1. Additionally support for the use of $im_{\lambda=0.55} = 0.0015i$ is that six estimates of ω_o for dust are available from the retrieval algorithm of *Dubovik and King* [2000] for the 25 September 2000 from Cape Verde. These retrievals suggest a mean $\omega_{o\lambda=0.441}$ of 0.96, and $\omega_{o\lambda=0.673}$ of 0.97 again suggesting that the absorption is significantly overestimated if *WCP* [1986] refractive indices are used.

[26] A density of 2.65 g cm^{-3} [e.g. *Haywood et al.*, 2001a] is used in estimation of the specific extinction coefficient, $k_{e\lambda=0.55}$, which is calculated as $0.42 \text{ m}^2\text{g}^{-1}$ and $0.33 \text{ m}^2\text{g}^{-1}$ for Dust A and Dust B size distributions. If mode 5 is excluded, $k_{e\lambda=0.55}$ rises to $0.70 \text{ m}^2\text{g}^{-1}$ and $0.74 \text{ m}^2\text{g}^{-1}$ for Dust A and Dust B. The effect of including mode 5 is thus to significantly reduce $k_{e\lambda=0.55}$, slightly decrease $g_{\lambda=0.55}$, and have little effect on $\omega_{o\lambda=0.55}$. The importance of mode 5 in determining the aerosol optical depth is also highlighted in Table 2 where it is shown to contribute over 30% to $\tau_{aer\lambda=0.55}$ for Dust A. The model calculations suggest that mode 5 would contribute to over 55% of $\tau_{aer\lambda=0.55}$ for Dust B but it should be stressed again that mode 5 is very poorly constrained for Dust B. As we shall see, the presence of large supermicron mode 5 particles has important consequences for determining $\tau_{aer\lambda=0.55}$ via in situ measurements of aerosol scattering and absorption (section 6.1).

6. Estimation of the Aerosol Direct Radiative Effect DRE and Aerosol Optical Depth $\tau_{aer\lambda}$ During Flight a797

[27] There are many ways in which $\tau_{aer\lambda}$ and DRE may be estimated from the measurements made by the C-130. Those investigated here are:-

[28] 1. Determination of $\tau_{aer\lambda}$ by integrating the scattering coefficient, $\sigma_{sca\lambda}$ and absorption coefficient, $\sigma_{abs\lambda}$ from the nephelometer and PSAP.

[29] 2. Determination of $\tau_{aer\lambda}$ from measurements of the downwelling broadband diffuse and direct components of the irradiance at low level [*Hignett et al.*, 1999].

[30] 3. Determination of the DRE and $\tau_{aer\lambda}$ from broadband measurements at high level [e.g. *Haywood et al.*, 2001a, 2001b].

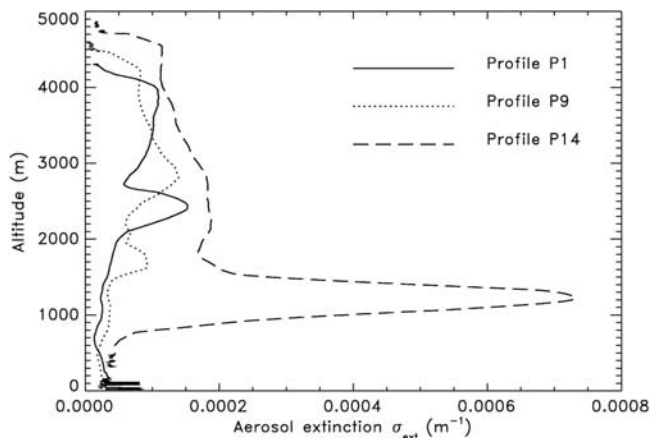


Figure 7. Profiles of $0.55 \mu\text{m}$ σ_{ext} , for profiles P1, P9, and P14 during flight a797 on 25 September 2000. σ_{ext} is derived from summing σ_{sca} and σ_{abs} . The data is smoothed using a running mean of 30 s. A correction factor of approximately 1.5 should be applied to σ_{ext} to account for scattering by supermicron aerosols that are missed by aerosol the inlet system (see text).

[31] 4. Determination of $\tau_{aer\lambda}$ by measuring the magnitude and the spectral dependence of the upwelling radiances at high levels with the SWS [e.g. Haywood *et al.*, 2003b].

[32] These approaches will be investigated in turn.

6.1. Determination of $\tau_{aer\lambda}$ by Integrating $\sigma_{sca\lambda}$ and $\sigma_{abs\lambda}$ From the Nephelometer and PSAP

[33] $\sigma_{sca\lambda}$ was measured by the nephelometer at wavelengths 0.45, 0.55, and 0.70 μm and $\sigma_{abs\lambda=0.567}$ were measured directly by the nephelometer and the PSAP during the profile ascents P1, P9, and P14. $\sigma_{sca\lambda=0.55}$ was added to $\sigma_{abs\lambda=0.567}$ to obtain the extinction coefficient at 0.55 μm , $\sigma_{ext\lambda=0.55}$. The vertical profiles of $\sigma_{ext\lambda=0.55}$ shown in Figure 7, show considerable variation with profiles P1 and P9 showing considerably lower values than P14 measured later in the day. P14 also shows a large peak of $\sigma_{ext\lambda=0.55}$ at altitudes of between 800 m and 1800 m ASL while the other two profiles show a more homogeneous nature. The back-trajectories [Tanré *et al.*, 2003] indicate that the dust at 1500 m may have traveled in from the north on a more northerly flow and may have originated in Mauritania rather than in the central Saharan regions. $\tau_{aer\lambda}$ may be obtained by integrating the vertical profile:-

$$\tau_{aer\lambda} = \int_0^z \sigma_{ext\lambda} dz. \quad (2)$$

[34] The results suggest $\tau_{aer\lambda=0.55}$ of 0.27, 0.30, and 0.85 for profiles P1, P9, and P14 respectively. As noted in section 4.1, laboratory measurements have shown that the collection efficiency of the Rosemount inlet is reduced for particle radii greater than 1 μm . In order to assess the effects of missing the large aerosol particles on the derived $\tau_{aer\lambda=0.55}$, Mie scattering calculations were performed using the Dust A distribution of section 4 to represent the aerosol size distribution. In the calculations, the tail of the distribution was progressively cut off to determine the effect on

the aerosol scattering and absorption coefficient, and hence $\tau_{aer\lambda=0.55}$. Figure 8 shows that both the absorption and scattering and consequently $\tau_{aer\lambda=0.55}$ will be significantly underestimated if the cutoff radius of the Rosemount inlet is between 1 and 2 μm . The degree of underestimation is difficult to determine, but can be estimated by comparison with τ_{aer} data from Sun photometers (section 7). $\tau_{aer\lambda=0.55}$ of 0.27 was measured for profiles P1 which was performed from Sal heading in a easterly direction toward Dakar for approximately 20 min duration from 10:00 UTC. $\tau_{aer\lambda=0.44}$ and $\tau_{aer\lambda=0.67}$ measured by the surface-based Sun photometers ranges from approximately 0.35 to 0.45 (see section 7) when accounting for the westward advection of the plume and the position of the aircraft. This suggests that $\tau_{aer\lambda=0.55}$ is underestimated by between a factor of 1.3 and 1.7 suggesting an inlet cutoff radius of between 1.3 and 1.9 μm . Applying a correction factor of 1.5 to account for the missing particles leads to $\tau_{aer\lambda=0.55}$ of 0.40, 0.45, and 1.28 for profiles P1, P9, and P14 respectively, but the uncertainty is considerable and is estimated as at least 30% leading to $\tau_{aer\lambda=0.55}$ of 0.40 ± 0.12 , 0.45 ± 0.14 , and 1.28 ± 0.38 . It is the fact that mineral dust contains large particles that contribute to the scattering at 0.55 μm that makes this method of determining $\tau_{aer\lambda=0.55}$ so uncertain. Haywood *et al.* [2003b] showed a much better constrained comparison against surface based Sun photometer measurements when considering smaller biomass burning aerosols. Future measurement campaigns will use a specially designed low turbulence inlet (LTI) to reduce this problem when measuring supermicron mineral dust particles. It was not possible to determine $\tau_{aer\lambda}$ from measurements of the particle concentration with the PCASP due to periodic noise problems at high altitudes within the dust layer during deep profile ascents and descents.

6.2. Determination of $\tau_{aer\lambda}$ by Measurements of the Direct and Diffuse Components of the Downwelling Broadband Radiation

[35] Down-Sun and into-Sun low-level SLRs (30 m ASL) were performed during R10.1 and R10.2 respectively (Figure 1). During R10.1 narrow pillar obscurers mounted

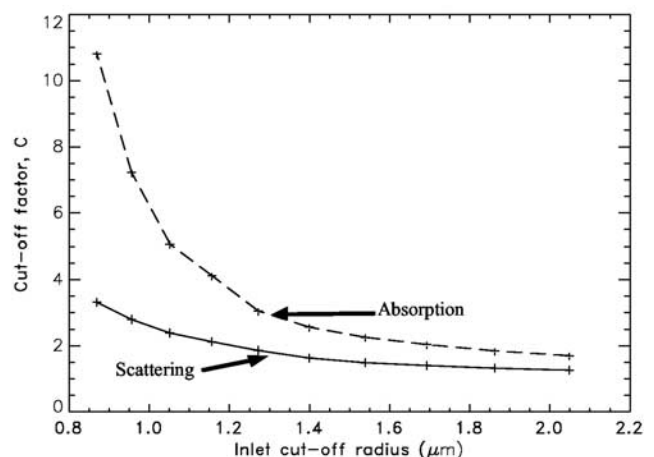


Figure 8. The cutoff factor C , which is the ratio of the scattering (absorption) with no inlet cutoff to the scattering (absorption) at the inlet cutoff radius.

directly aft of the upper pyranometers shadow the pyranometer thermopile so it responds only to the downward diffuse irradiance. This enables the modeled direct and diffuse components of the downward irradiances to be compared against the pyranometer measurements [e.g. *Hignett et al.*, 1999; *Haywood et al.*, 2001a]. A correction to the diffuse component of the measured downward irradiance accounts for the fraction of the forward-scattered diffuse component being blocked by the obscurers. This correction relies on knowledge of the radiance field i.e. the directional dependence of the radiation. As in the work by *Hignett et al.* [1999], SAFIRE radiance data from banked orbits (Figure 1) is used to determine the radiance distribution. The derived direct fluxes can then be compared to model calculations without aerosol to derive broadband values of $\tau_{aer\lambda}$. These measurements suggest broadband optical depths $\tau_{aer\lambda=0.3-0.7}$ of 0.94, and $\tau_{aer\lambda=0.7-3.0}$ of 0.81. The measured direct irradiances have an estimated accuracy of around 8% [*Haywood et al.*, 2001a], which leads to an estimated error in $\tau_{aer\lambda=0.3-0.7}$ and $\tau_{aer\lambda=0.7-3.0}$ of approximately 8%. $\tau_{aer\lambda=0.55}$ may be estimated by performing radiative transfer calculations with the *Edwards and Slingo* [1996] radiation code to determine the aerosol burden that needs to be applied to the model atmosphere so that the measured 0.3–3.0 μm direct irradiance matches the modeled direct irradiance. The aerosol optical properties for Dust A determined in section 5.2 are used as input to the radiation code. The results suggest a $\tau_{aer\lambda=0.55}$ of 0.88. The error associated with this estimate is higher than 8% owing to the additional uncertainty associated with the modeling of the spectral dependency of the aerosol optical parameters. The overall error is estimated to be at least 10%, thus $\tau_{aer\lambda=0.55}$ of 0.88 ± 0.09 provides an estimate of the aerosol optical depth obtained from this method.

6.3. Determination of the DRE and $\tau_{aer\lambda}$ by Measurements With the BBRs at High Level

[36] This method has previously been used by *Haywood et al.* [2001a, 2001b] to estimate the optical depth of Saharan dust from flights at fixed longitude over the entire dust plume during April/May 1999. The upwelling irradiances at a level (~ 1000 m) above the aerosol layer are measured by the downward facing BBRs. A 4-stream version of the *Edwards and Slingo* [1996] radiation code is used together with a combination of the broadband sea-surface reflectance parameterization of *Glew et al.* [2003] and the sea-surface angular scattering parameterization detailed by *Thomas and Stammes* [1999]. The radiation code is then used to model the upwelling irradiance excluding aerosol from the calculations, $Uflx_{no_aer}$. Increasing $\tau_{aer\lambda}$ with the mean optical properties derived from the Dust A size distribution is then included in calculations until the upwelling irradiance matches the measured irradiance, $Uflx_{aer}$. These calculations are performed over the range of solar zenith angles measured during the flight. Only the results obtained from R6 and R11 are presented here as during these runs the solar zenith angle, θ , was relatively modest (R6: $\theta = 17.6^\circ-18.8^\circ$, R11: $\theta = 35.4^\circ-38.7^\circ$) and well characterized by the *Glew et al.* [2003] surface reflectance parameterization which is based on BBR measurements by the C-130. During R19 θ varied between 70.3° and

75.6° : at these large solar zenith angles, the surface reflectance is not well characterized making determination of the DRE and $\tau_{aer\lambda}$ subject to larger uncertainties. The solar DRE, is simply:

$$\text{DRE} = Uflx_{no_aer} - Uflx_{aer}. \quad (3)$$

[37] $Uflx_{no_aer}$ and $Uflx_{aer}$ are shown in Figure 9a by the dashed and solid lines respectively, DRE is shown in Figure 9b, and the derived $\tau_{aer\lambda=0.55}$ is shown in Figure 9c. The model calculations show that DRE at the level of the C-130 (R6: 5227 m standard deviation 6 m; R11: 4893 m standard deviation 3 m) is an accurate representation of DRE at the top of the atmosphere or the tropopause as the DRE evaluated at these levels differs by less than 0.2 Wm^{-2} .

[38] $Uflx_{no_aer}$ shows very little variation ($49.2-49.9 \text{ Wm}^{-2}$) owing to the competing effects of the surface reflectance and solar zenith angle [*Haywood et al.*, 2001a, 2001b]. $Uflx_{aer}$ however, shows considerable longitudinal variation with values reaching a maximum of 179.1 Wm^{-2} close to the eastern end of R6. There is also evidence of the westward advection of the aerosol plume as R11 shows higher values of $Uflx_{aer}$ than colocated measurements during R6. Figure 9b shows that the DRE ranges from -44.0 Wm^{-2} at the western end of R6 to -129.2 Wm^{-2} at the eastern end. It should be re-iterated here that the DRE is independent of assumed aerosol properties. This is because $Uflx_{aer}$ is measured, and $Uflx_{no_aer}$ is derived from radiative transfer calculations excluding aerosol.

[39] $\tau_{aer\lambda=0.55}$ is calculated to range from 0.48 to 1.48, and shows an almost constant value of 0.52 ± 0.01 between longitudes of -22.5° and -20.5° for R6. For R11, $\tau_{aer\lambda=0.55}$ ranges from 0.81 at the western end to 1.10 at the eastern end. The normalized DRE, NDRE may be computed by dividing the DRE by $\tau_{aer\lambda=0.55}$ or by the column burden of aerosol. The NDRE calculated this way leads to -87 to $-98 \text{ Wm}^{-2}/\tau_{aer\lambda=0.55}$ or, assuming a $k_{e\lambda=0.55}$ of $0.42 \text{ m}^2\text{g}^{-1}$ (Table 2) -207 to -233 Wg^{-1} . These values are higher than those reported in *Haywood et al.* [2001b] who reported values of NDRE of between $-36 \text{ Wm}^{-2}/\tau_{aer\lambda=0.55}$ and $-76 \text{ Wm}^{-2}/\tau_{aer\lambda=0.55}$ or -53 to -112 Wg^{-1} . Two factors are responsible for these discrepancies. First, the inclusion of a fifth lognormal mode reduces $k_{e\lambda=0.55}$ in the calculations presented here. Second, *Haywood et al.* [2001b] determined a significantly lower $\omega_{o\lambda=0.55}$ is due to the neglect of scattering and absorption corrections for the nephelometer and PSAP and due to the mixing of aerosol from biomass burning with the dust aerosol during April/May 1999. Measurements of CO during those flights suggested a good correlation of CO with PCASP number concentration and σ_{sca} from the nephelometer: this correlation was not consistently evident during the SHADE flights. On occasion some correlation was observed, but on the basis of NO_3 to non sea-salt SO_4 ratios, this is attributed to distant anthropogenic pollution from Europe rather than biomass burning [*Formenti et al.*, 2003]. *Haywood et al.* [2001b] suggested that the model and measurements were each uncertain to $\pm 5 \text{ Wm}^{-2}$ leading to an estimated error in the DRE of $\pm 7 \text{ Wm}^{-2}$ (RMS error). However, in this case, the errors in the model are likely significantly less than $\pm 5 \text{ Wm}^{-2}$,

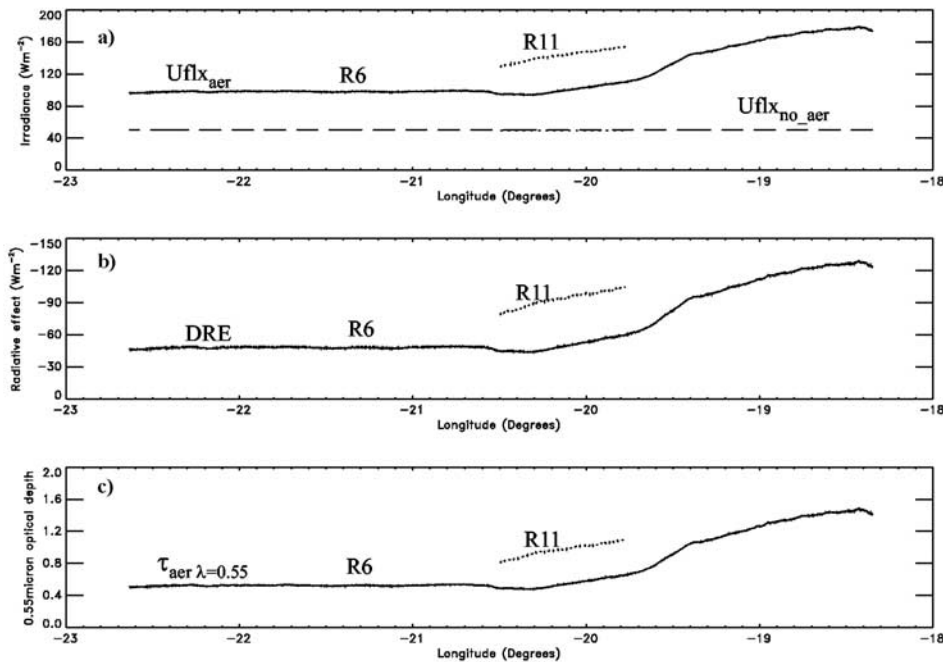


Figure 9. (a) The modeled $Uflx_{no_aer}$ (dashed line), and measured $Uflx_{aer}$ 0.3–3.0 μm irradiance (solid and dotted lines). (b) The direct radiative effect DRE. (c) The aerosol optical depth, $\tau_{aer\lambda=0.55}$. In each case the solid line represents measurements and calculations from R6 and the dotted line measurements and calculations from R11.

because the atmospheric humidity is intensively characterized by dropsondes and aircraft profiles. We estimate the uncertainty in the modeled irradiance (without aerosol) as no more than $\pm 2 \text{ Wm}^{-2}$ and therefore consider the DRE to be dominated by the errors in the measurements at $\pm 5 \text{ Wm}^{-2}$. An error of $\pm 5 \text{ Wm}^{-2}$ translates to an estimated error in $\tau_{aer\lambda=0.55}$ of ± 0.05 .

[40] It is straightforward to compute the maximum fractional increase in the reflected radiation at the level of the aircraft due to the presence of aerosols as simply $Uflx_{aer}/Uflx_{no_aer} = 3.6 \pm 0.1$. The maximum increase in the local planetary albedo is assessed by considering the corresponding ratio of the modeled upwelling irradiances at the top of the atmosphere when aerosols are included and excluded from the radiative transfer calculations. The calculations reveal an enhancement of the local planetary albedo over ocean by a factor of 2.7 ± 0.1 . Similar measurements made off the coast of Angola/Namibia during the peak of the S. African biomass burning season during SAFARI2000 [Haywood *et al.*, 2003b] reveal a more modest increase in planetary albedo of 1.4 ± 0.1 suggesting that Saharan dust events exert a significantly stronger perturbation to the top of atmosphere local radiation budget than biomass smoke.

[41] It is also possible to estimate the change in the downwelling irradiance at the surface from the measurements and radiative transfer modeling efforts. For the greatest DRE of -129 Wm^{-2} during R6, the corresponding reduction at the surface was calculated to be approximately -209 Wm^{-2} or a factor of approximately 1.6 greater than the top of the atmosphere DRE. This ratio is smaller than that calculated by Haywood *et al.* [2001a]

who calculated approximately a factor of 3 for similar values of θ , mainly due to the higher value of ω_o in the present study.

6.4. $\tau_{Aer\lambda}$ by Measuring the Magnitude and Spectral Distribution of the Upwelling Radiance

[42] Here, the SWS instrument is used in place of the BBRs to estimate the spectral dependence and magnitude of the surface reflectance from the low-level runs (R10), and this is used in modeling the upwelling radiance for the high level SLRs [Haywood *et al.*, 2003b]. The area of relatively constant $\tau_{aer\lambda=0.55}$ during R6 between longitudes of -20.5° to -22.5° is focused on to reduce uncertainties in the calculations due to variability in the dust loading. The mean measured nadir view radiance at low level (R10) is modeled using the *Edwards and Slingo* [1996] radiation code by adjusting the spectral dependence of a Lambertian surface reflectance, R_s , until the measured and modeled radiances agree. A constant aerosol mass mixing ratio vertical profile of aerosol is included between 950 and 600 hPa using the optical parameters derived from the Dust A size distribution. The aerosol concentration is then adjusted so that the best agreement is found between the measured and modeled nadir view radiance during the high level SLR (R6). This method involves a degree of iteration: (1) guess the aerosol mass loading (initially $\tau_{aer\lambda=0.55} = 0.52$); (2) guess the surface reflectance (initially 0.05); (3) calculate the upwelling radiance at low level; (4) compare the results from step 3 against the measurements; (5) adjust the surface reflectance so that the upwelling radiances at low level agree; (6) calculate the upwelling radiance for high-level SLR; (7) compare the modeled upwelling radiance at high level to

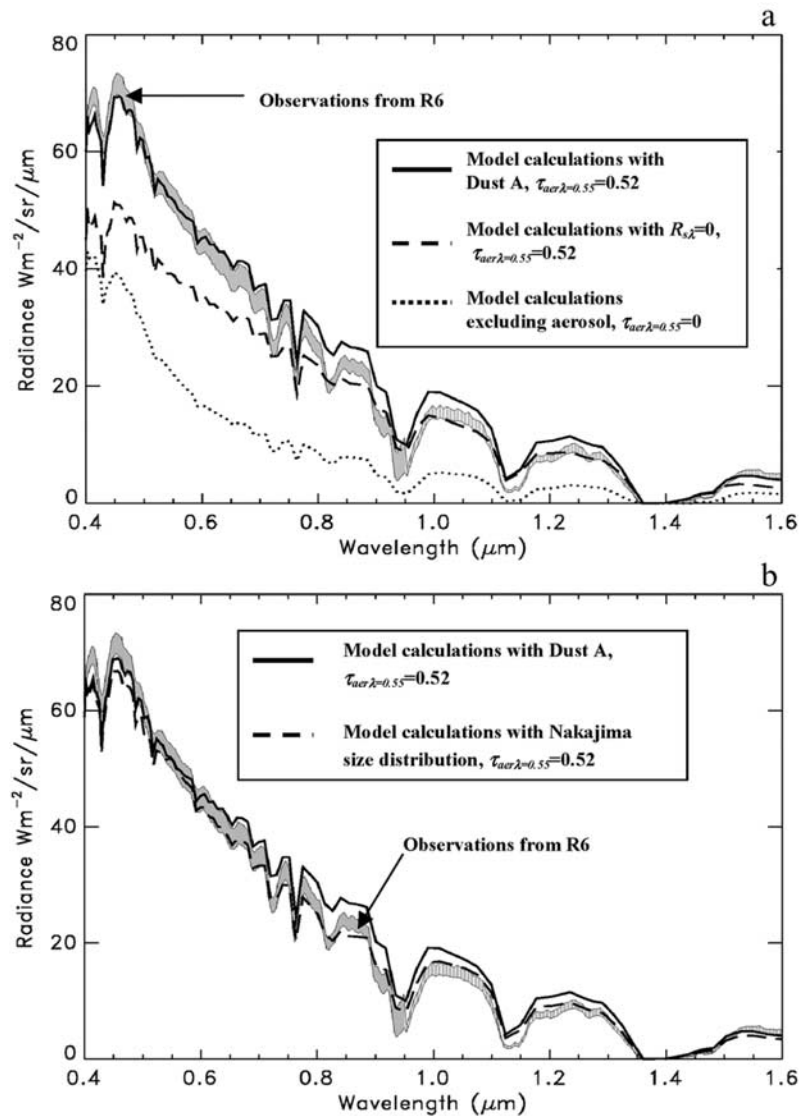


Figure 10. (a) The observed nadir radiances measured by the SWS instrument on the C-130 (gray envelope). Model calculations with $\tau_{aer\lambda=0.55} = 0.52$ (solid black line), $\tau_{aer\lambda=0.55} = 0$ (dotted black line), and $\tau_{aer\lambda=0.55} = 0.52$ but with $R_{s\lambda}$ reduced to zero (dashed black line) are also shown. (b) As in Figure 9b, but with the dashed line representing the radiance modeled using the Nakajima size distribution.

that measured; (8) adjust the aerosol optical depth; and (9) use the new R_s and $\tau_{aer\lambda}$ in steps 3–7.

[43] An assumption implicit within the calculations is that the surface may be modeled using a Lambertian reflector and that the nature of the bidirectional reflection distribution function (BRDF) is such that the surface reflectance does not change significantly between the R10 ($\theta = 28.1^\circ$), and R6 ($\theta = 17.6^\circ - 18.8^\circ$). The calculation presented here are entirely consistent for $\tau_{aer\lambda=0.55} = 0.52$ and therefore steps 8 and 9 do not need to be performed. The results from the calculations are shown in Figure 10.

[44] The measurements from the SWS instrument are shown by the gray envelope (mean radiance ± 2 standard deviations). The results show that the measured upwelling radiances are well-represented (within 2 standard deviations)

in the wavelength range 0.45–0.65 μm wavelengths when $\tau_{aer\lambda=0.55} = 0.52$. In addition to these calculations, calculations are also performed for an atmospheric column excluding aerosol, and a spectrally independent zero surface reflectance. As expected, both of these calculations show reduced upwelling radiance. The fact that adjusting the surface reflectance to zero has a relatively large effect upon the upwelling radiance means that the surface reflectance has to be modeled reasonably accurately.

[45] For the calculations including the Dust A aerosol, statistically significant differences occur between the measured and modeled radiances in the wavelength range 0.65–1.4 μm before reasonable agreement is again found at wavelengths in excess of 1.5 μm. Reasons for these differences may lie in errors in the aerosol size distribution,

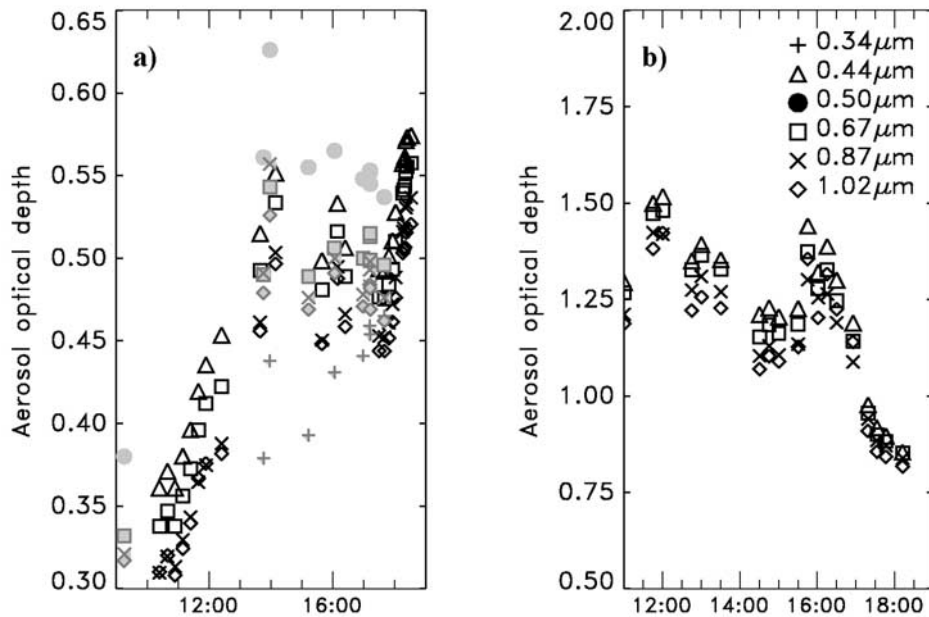


Figure 11. τ_{aer} derived from the AERONET ($\lambda = 0.44 \mu\text{m}$, $0.67 \mu\text{m}$, $0.87 \mu\text{m}$, and $1.02 \mu\text{m}$) and microtops ($\lambda = 0.34 \mu\text{m}$, $0.50 \mu\text{m}$, $0.67 \mu\text{m}$, and $1.02 \mu\text{m}$) Sun photometers on 25 September 2000. (a) Cape Verde and (b) Dakar. The microtops data is shown in gray in Figure 11a. Note the different scales in Figures 11a and 11b.

surface reflectance, refractive indices, or errors caused by the assumption of spherical particles. A size distribution derived from measurements made solely during flight a797 from SLRs R2, R3, R4 was also used as this aerosol should be most representative of the aerosol overflown during R6. However, little improvement in agreement between the spectral dependence of observed and modeled radiances was noted. In addition, calculations were also performed using the column averaged aerosol size distribution derived from the *Nakajima et al.* [1996] retrieval (Figure 6). Figure 10b shows that the radiances at $0.55 \mu\text{m}$ are still well represented when $\tau_{\text{aer}\lambda=0.55} = 0.52$. The spectral dependence of the modeled radiance is in better agreement than when using the Dust A size distribution. Examination of the wavelength dependence of $k_{e\lambda}$ shows a larger reduction as λ increases in the $0.5\text{--}1.5 \mu\text{m}$ spectral region for the *Nakajima et al.* [1996] retrieval, than for the Dust A case.

[46] Nevertheless, the fact remains that a $\tau_{\text{aer}\lambda=0.55}$ of 0.52 is entirely consistent with the measurements made with the BBRs. The error in $\tau_{\text{aer}\lambda=0.55}$ is estimated as ± 0.04 .

7. Comparison of τ_{aer} From Aircraft With Those From Surface Observations

[47] Surface observations of τ_{aer} are available for 25 September from the AERONET Sun photometer network (<http://aeronet.gsfc.nasa.gov>) at both Cape Verde and Dakar, and from measurements made by microtops Sun photometers at Cape Verde. The measurements of $\tau_{\text{aer}\lambda}$ are shown in Figure 11. At Cape Verde, $\tau_{\text{aer}\lambda}$ increases as the morning progresses and is relatively stable between 13:00 and 18:00 UTC before showing a significant increase later in the evening. $\tau_{\text{aer}\lambda=0.55}$ may be estimated from the AERONET and microtops wavelengths by assuming that $\tau_{\text{aer}\lambda}$ varies

linearly between the $0.44\text{--}0.67 \mu\text{m}$ for the AERONET Sun photometers and $0.50\text{--}0.67 \mu\text{m}$ for the microtops Sun photometer. The errors introduced by this assumption are small at approximately ± 0.01 because the variation in $\tau_{\text{aer}\lambda}$ is not as strongly wavelength dependent as for other aerosols such as industrial pollution or biomass aerosol. During the period 13:00–18:00 UTC, $\tau_{\text{aer}\lambda=0.55}$ was 0.50 (standard deviation 0.02), and 0.54 (standard deviation 0.03) for the AERONET and Microtops Sun photometers respectively. Comparisons against $\tau_{\text{aer}\lambda}$ from the aircraft measurements are possible during this stable period. $\tau_{\text{aer}\lambda=0.55}$ from measurements of upwelling irradiance with BBRs (section 6.3), from R6 at 13:20 UTC is 0.52 ± 0.05 which is entirely consistent with the Sun photometer data. The data obtained from the SWS during R6 (section 6.4) gives a $\tau_{\text{aer}\lambda=0.55}$ of 0.52 ± 0.04 which is also entirely consistent with the Sun photometer data.

[48] At Dakar, only three level 2 quality-controlled data points are available from the AERONET site for 25 September, so we rely on the less rigorously quality controlled level 1 data. The data shows peak $\tau_{\text{aer}\lambda=0.55}$ values of 1.48–1.49 just before 12:00 UTC. The peak $\tau_{\text{aer}\lambda=0.55}$ from measurements of the upwelling irradiance with the BBRs (section 6.3) occurs near the Dakar end of R6 where a peak $\tau_{\text{aer}\lambda=0.55}$ of 1.48 ± 0.05 is obtained at approximately 12:30 UTC. Once again, the aircraft measurements and the Sun photometer measurements are entirely in agreement.

8. Comparison of C-130 Derived Direct Radiative Effect DRE With That Derived From Satellite Instruments

[49] In this study, data from the CERES satellite instrument [*Wielicki et al.*, 1996] is compared against that derived

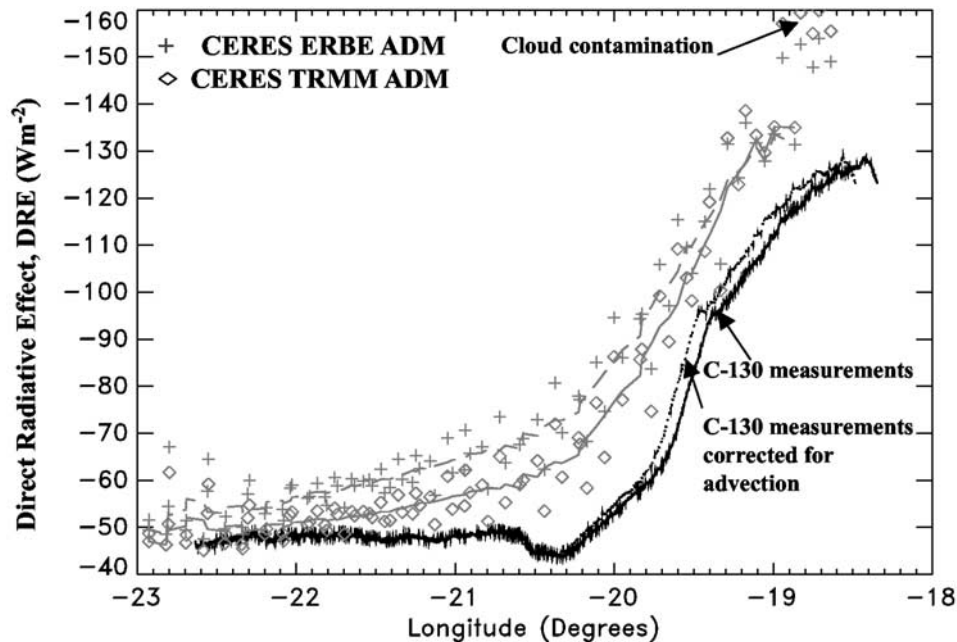


Figure 12. Comparison of direct radiative effect from CERES and from the C-130 plotted as a function of longitude. The CERES data is restricted to data points less than 75 km from the C-130 flight path. The plus signs represent the direct radiative effect when using the ERBE ADM, and the diamonds represent the direct radiative effect using the TRMM ADM. The dashed and solid gray lines shows 6-point running means of the direct radiative effect obtained using the ERBE and TRMM ADMs respectively. The estimated error in the direct radiative effect from the C-130 measurements is $\pm 5 \text{ W m}^{-2}$. The UTC times of the C-130 measurements are shown at each end of R6. The CERES measurements were made at 13:00 UTC.

from the aircraft measurements. The CERES instantaneous DRE of aerosols at the top-of-atmosphere (TOA) at latitude ϕ and longitude ψ is determined in an analogous manner to the aircraft measurements of section 5.3 as follows:

$$DRE(\theta_o, \phi, \psi) = Uflx_{no_aer}(\theta_o, \phi, \psi) - Uflx_{aer}(\theta_o, \phi, \psi),$$

where $Uflx_{aer}(\theta_o, \phi, \psi)$ is the instantaneous shortwave radiative irradiance inferred from satellite radiance measurements, and $Uflx_{no_aer}(\theta_o, \phi, \psi)$ is the irradiance when no aerosols are present. $Uflx_{aer}(\theta_o, \phi, \psi)$ is estimated from CERES solar radiance measurements by applying empirical angular distribution models (ADM) consisting of anisotropic correction factors that relate radiances in any Sun-Earth-satellite viewing geometry to TOA SW irradiances. In this study, two sets of ADMs are used. The CERES/TRMM ADMs are determined from 9 months of coincident CERES and Visible Infrared Scanner (VIRS) measurements from the Tropical Rainfall Measuring Mission (TRMM) satellite. The ERBE ADMs are the operational ADMs used in the Earth Radiation Budget Experiment [Smith *et al.*, 1986] which have been applied to CERES data (CERES “ERBE-Like” product) [Wielicki *et al.*, 1996]. $Uflx_{no_aer}(\theta_o, \phi, \psi)$ is estimated from the intercept of a regression between $Uflx_{aer}(\theta_o, \phi, \psi)$ and aerosol optical depth retrievals from VIRS. A more detailed description of the methodology for evaluating the terms in equation (1) is provided in the work of Loeb and Kato [2002].

[50] It should be noted that the scene identification algorithm employed by the CERES ERBE-Like product suggests that every point in the comparison is “partly cloudy” while

the aircraft observations suggest the presence of large quantities of dust but no cloud. The more advanced CERES product, known as the “Single Satellite Footprint TOA/Surface Fluxes and Clouds (SSF) product,” combines CERES and imager data (VIRS on TRMM; MODIS on Terra and Aqua) to identify the scene type. The CERES/TRMM ADMs were constructed using the more advanced CERES SSF product. Unfortunately, the CERES/Terra SSF product for September 2000 is not yet available for comparison with the aircraft observations. In applying the CERES/TRMM ADMs, therefore, the region is assumed to be cloud free.

[51] Estimates of the DRE of aerosols were determined for 25 September 2000 over 13°N – 18.5°N and 19°W – 23°W using CERES measurements from the Terra spacecraft. The measurements were acquired at approximately 13:00 UTC. Solar zenith angles ranged from 15° – 20° , viewing zenith angles were between 55° and 70° , and relative azimuth angles were between 60° and 70° .

[52] The CERES data is restricted to points that are less than 75 km from the track of the C-130 aircraft. Additional comparisons restricting data to within 100 km show and 50 km show similar results to those shown here. The C-130 DRE data is restricted to R6 between 12:26:00 and 13:20:00 UTC. This means that the aircraft and satellite data are concurrent to approximately 35 min accuracy. Cumulus cloud was reported by the aircraft scientist beyond the eastern end of R6, and so it is likely that five of the CERES points may be affected by cloud contamination. These are excluded from the running mean of the CERES data.

[53] Figure 12 shows that the general geographical dependence of the CERES data is in reasonable agreement

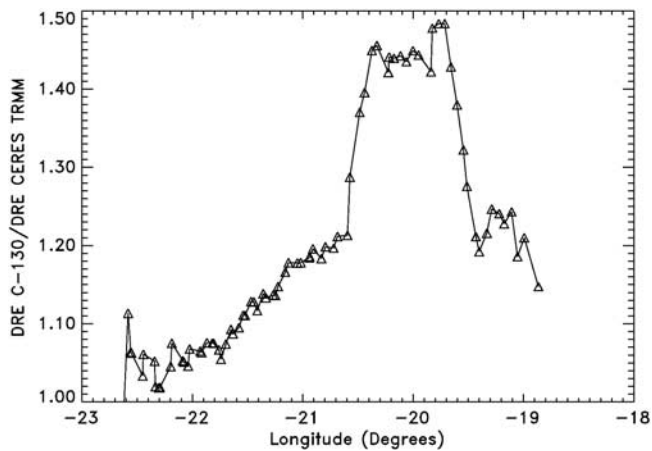


Figure 13. The ratio of the DRE derived from CERES TRMM ADM to that derived from the C-130 BBRs.

with that from the C-130. The TRMM ADM gives results that are in closer agreement to the C-130 measurements, indicating that this ADM performs somewhat better in this case. The C-130 and CERES/TRMM radiative effect are within the C-130 estimated error of $\pm 5 \text{ Wm}^{-2}$ westward of approximately 21.5°W . Eastward of this point, the differences between the C-130 and CERES/TRMM estimates of the DRE increase. The possibility of the westward advection of the aerosol accounting for differences between the derived DREs is investigated. The mean easterly wind speed in the 950–600 hPa layer from three (the parachute failed on one) dropsondes launched during R6 to be approximately 7.4 ms^{-1} . The longitude of the DRE was adjusted according to the time difference between the CERES and C-130 observations assuming simple easterly advection. As seen in Figure 12, advection is unlikely to account for the differences observed between CERES and the C-130. The difference in the footprint size may account for some of the differences, particularly as there is such a steep gradient in the DRE between 20°W and 19°W . Taking into account to cosine weighting of the BBR instruments on the C-130, and considering that R6 was performed at an altitude of approximately 5000 m, 95% of the signal comes from a circular foot-print with diameter of 30 km. For CERES viewing zenith angles between 55° and 70° , the foot-print size of CERES is equivalent to a circle diameter that ranges from 45 km to 83 km. This means that the DRE from CERES is likely to be somewhat smoother across large gradients than that derived from BBR measurements on the C-130. Other differences may be caused by possible north/south gradients in the dust plume.

[54] Nevertheless, Figure 13 shows that the difference between the DRE from CERES/TRMM ADM and that from the C-130 BBR measurements is never greater than a factor of 1.5. Westward of 21°W , where the gradient in DRE is not strong the difference between the retrievals is less than a factor of 1.2. This suggests that the CERES estimates of DRE from Saharan dust is relatively well represented.

9. Discussion and Conclusions

[55] During the strong Saharan dust outbreak measured during a796, a797 and a798, the size distribution measured

by the PCASP-100X contained proportionally a greater number of large particles. It is not possible from the measurements to definitively attribute the increase in the large particles to the age of the plume or different source characteristics. The submicron particles measured by the PCASP-100X during the entire campaign may be represented by the sum of 4 lognormal modes. However, a significant proportion of the mass of the mineral dust aerosol exists in a fifth mode with a mode radius (by number) of $1.8 \mu\text{m}$. The failure of the FFSSP instrument means that size distributions determined by surface-based Sun photometry have to be relied upon to give reasonable estimates of supermicron sized particles.

[56] The optical parameters are determined by measurements of absorption and scattering coefficients with the PSAP and nephelometer respectively that are corrected for absorption artifacts and for truncation of the scattered radiation. The results suggest that $\omega_{0\lambda=0.55}$ is in the range 0.95 to 0.99. To achieve these values, $im_{\lambda=0.55}$ needs to be adjusted from the WCP [1986] value of $0.008i$ to $0.0015i$. These results support the growing body of evidence that the refractive indices used in global modeling studies are in error, and that the absorption by mineral dust has been overestimated. This evidence includes the data from Sun photometer measurements during SHADE where a mean $\omega_{0\lambda=0.441}$ of 0.96, and $\omega_{0\lambda=0.673}$ of 0.97 were inferred. Additionally, Kaufman *et al.* [2001] used remote sensing to infer an $\omega_{0\lambda=0.55}$ of 0.97 for Saharan dust. The absorption due to mineral dust may not have been overestimated solely for Saharan dust: Clarke *et al.* [2001] made aircraft observations of dust transported from Asia using identical instrumentation to that used on the C-130, and found an $\omega_{0\lambda=0.55}$ of 0.97. The $\omega_{0\lambda=0.55}$ of 0.87 reported by Haywood *et al.* [2001a] for Saharan dust is likely to be too low because the corrections to the nephelometer scattering and absorption were not applied and because of possible mixing of the Saharan dust with biomass aerosol. A reassessment of $\omega_{0\lambda=0.55}$ from that flight reveals $\omega_{0\lambda=0.55}$ of 0.94.

[57] These results have important implications in estimates of the direct radiative forcing i.e. the change in net solar radiation anthropogenic component of mineral dust in the atmosphere. Myhre *et al.* [2003] investigates the radiative impact of the mineral dust aerosol event measured in this paper on regional and global scales, and deduces that the solar radiative forcing is more strongly negative (by approximately a factor of two) than estimates with WCP [1986] refractive indices. Myhre *et al.* [2003] conclude that the effect of mineral emissions from the Sahara results in a globally mean diurnally averaged net (solar plus terrestrial) direct radiative effect of -0.4 Wm^{-2} . Ramaswamy *et al.* [2001] assess the direct radiative forcing due to mineral dust as lying between -0.6 Wm^{-2} and $+0.4 \text{ Wm}^{-2}$, the positive forcings resulting from a combination of absorption of solar and terrestrial radiation. However, given the number of results that are now showing reduced solar absorption by mineral dust, the possibility of a global mean positive radiative forcing appears unlikely.

[58] $\tau_{aer\lambda}$ is estimated in a number of different ways for flight a797. $\tau_{aer\lambda}$ showed significant spatial and temporal variation as the large dust plume was advected westward. Such temporal and spatial variations make definitive conclusions about the accuracy of the methods somewhat

problematic. However, it is clear that the method of integrating the scattering and absorption coefficients from the nephelometer and PSAP underestimates $\tau_{aer\lambda}$. The reasons for this is very likely due to the inlet collection efficiency dropping from close to unity to close to zero for particle radii greater than 1–2 μm . An approximate correction may be applied to account for the missing particles, but $\tau_{aer\lambda=0.55}$ derived from this method is subject to an uncertainty of at least 30%. The radiometric measurements of $\tau_{aer\lambda=0.55}$ show significantly better consistency with each other and better agreement with the Sun photometer derived values. Measurements of the upwelling irradiance with the BBRs suggest $\tau_{aer\lambda=0.55} = 0.52 \pm 0.05$ over a large geographical area during R6. These results are entirely consistent with those obtained from measurements of the upwelling radiance by the SWS instrument which yield $\tau_{aer\lambda=0.55} = 0.52 \pm 0.04$. The measured and modeled spectral dependence of the radiance differ to some degree, which is likely due to some errors in the measured size distribution, and the fact that the PCASP size distribution is representative of the dust aerosol layer, rather than the column integrated aerosol size distribution, or nonspherical scattering effects.

[59] $\tau_{aer\lambda=0.55}$ of 0.88 ± 0.09 is derived from measurements of the downwelling irradiance close to the surface. It is apparent from the BBR measurements during R11 that $\tau_{aer\lambda=0.55}$ was starting to increase due to the westward advection of the dust plume. The minimum value of $\tau_{aer\lambda=0.55}$ during R11 derived from measurements of the upwelling irradiance is 0.81 ± 0.05 , so these results are consistent within the estimated errors.

[60] The radiometric measurements of $\tau_{aer\lambda}$ are shown to be entirely consistent with the AERONET measurements of $\tau_{aer\lambda}$ made at Sal and Dakar during flight a797 [Dubovik et al., 2000]. The comparison of the aerosol DRE measured by the C-130 with those derived from the CERES/TRMM ADM is used. The results generally show consistency within a factor of 1.2 except where there are strong gradients in the aerosol DRE.

[61] The results show that, for Saharan dust plumes near the source region, $\tau_{aer\lambda=0.55}$ can reach approximately 1.5, and the upwelling irradiance or planetary albedo may be enhanced by up to a factor of 2.7 ± 0.1 . There is no reason to suppose that this particular dust event was an unusually large phenomena, and thus the effect of Saharan dust plumes on the local, regional, and even global radiation budget must be considered important.

[62] **Acknowledgments.** Thanks are due to Jon Taylor and Tad Anderson for reading an earlier version of the manuscript. The crew and support staff of the Met Office MRF are thanked for their efforts during and after the measurement campaign. P. Formenti acknowledges funding support from the German Max Planck Society.

References

- Anderson, T. L., and J. A. Ogren, Determining aerosol radiative properties using the TSI 3563 integrating nephelometer, *Aerosol Sci. Technol.*, 29, 57–69, 1998.
- Bond, T. C., T. L. Anderson, and D. Campbell, Calibration and intercomparison of filter-based measurements of visible light absorption by aerosols, *Aerosol Sci. Technol.*, 30, 582–600, 1999.
- Clarke, A. D., W. G. Collins, P. J. Rasch, V. N. Kapustin, K. Moore, S. Howell, and H. E. Fuelberg, Dust and pollution transport on global scales: Aerosol measurements and model predictions, *J. Geophys. Res.*, 106, 32,555–32,569, 2001.
- Dubovik, O., and M. King, A flexible inversion algorithm for retrieval of aerosol optical properties from Sun and sky radiance measurements, *J. Geophys. Res.*, 105, 20,673–20,696, 2000.
- Dubovik, O., A. Smirnov, B. N. Holben, M. King, Y. J. Kaufman, T. F. Eck, and I. Slutsker, Accuracy assessment of aerosol optical properties retrieval from AERONET Sun and sky radiance measurements, *J. Geophys. Res.*, 105, 9791–9806, 2000.
- Dubovik, O., B. N. Holben, T. Lapyonok, A. Sinyuk, M. I. Mishchenko, P. Yang, and I. Slutsker, Non-spherical aerosol retrieval method employing light scattering by spheroids, *Geophys. Res. Lett.*, 29(10), 1415, doi:10.1029/2001GL014506, 2002.
- Edwards, J. M., and A. Slingo, Studies with a flexible new radiation code. I: Choosing a configuration for a large scale model, *Q. J. R. Meteorol. Soc.*, 122, 689–720, 1996.
- Foot, J. S., A new pyrgeometer, *J. Atmos. Oceanic Technol.*, 3, 363–370, 1986.
- Formenti, P., W. Elbert, W. Maenhaut, J. M. Haywood, and M. O. Andreae, Chemical composition of mineral dust aerosol during the Saharan Dust Experiment (SHADE) airborne campaign in the Cape Verde region, September 2000, *J. Geophys. Res.*, 108(D18), doi:10.1029/2002JD002648, in press, 2003.
- Francis, P. N., P. Hignett, and J. P. Taylor, Aircraft observations and modeling of sky radiance distributions from aerosol during TARFOX, *J. Geophys. Res.*, 104, 2309–2319, 1999.
- Glew, M. D., P. Hignett, and J. P. Taylor, Aircraft measurements of sea surface albedo, *J. Atmos. Sci.*, in press, 2003.
- Haywood, J. M., and S. R. Osborne, Corrections to be applied to the PSAP and nephelometer for accurate determination of the absorption coefficient, scattering coefficient and single scattering albedo, *MRF Tech. Note 31*, Met Office, Bracknell, UK, 2000.
- Haywood, J. M., V. Ramaswamy, and B. J. Soden, Tropospheric aerosol climate forcing in clear-sky satellite observations over the oceans, *Science*, 283, 1299–1305, 1999.
- Haywood, J. M., P. N. Francis, M. D. Glew, and J. P. Taylor, Optical properties and direct radiative effect of Saharan dust: A case study of two Saharan outbreaks using data from the U.K. Met Office C-130, *J. Geophys. Res.*, 106, 18,417–18,430, 2001a.
- Haywood, J. M., P. N. Francis, I. Geogdzhayev, M. Mishchenko, and R. Frey, Comparison of Saharan dust aerosol optical depths retrieved using aircraft mounted pyranometers and 2-channel AVHRR algorithms, *Geophys. Res. Lett.*, 28(12), 2393–2396, 2001b.
- Haywood, J., S. R. Osborne, P. N. Francis, A. Keil, P. Formenti, M. O. Andreae, and P. H. Kaye, The mean physical and optical properties of regional haze dominated by biomass burning aerosol measured from the C-130 aircraft during SAFARI 2000, *J. Geophys. Res.*, 108(D13), 8473, doi:10.1029/2002JD002226, 2003a.
- Haywood, J., P. Francis, O. Dubovik, M. Glew, and B. Holben, Comparison of aerosol size distributions, radiative properties, and optical depths determined by aircraft observations and Sun photometers during SAFARI 2000, *J. Geophys. Res.*, 108(D13), 8471, doi:10.1029/2002JD002250, 2003b.
- Hess, M., P. Koepke, and I. Schult, Optical properties of aerosols and clouds: The software package OPAC, *Bull. Am. Meteorol. Soc.*, 79, 831–844, 1998.
- Highwood, E. J., J. M. Haywood, M. Silverstone, S. M. Newman, and J. P. Taylor, Radiative properties and direct effect of Saharan dust measured by the C-130 aircraft during Saharan Dust Experiment (SHADE). 2: Terrestrial spectrum, *J. Geophys. Res.*, 108(D18), doi:10.1029/2002JD002552, in press, 2003.
- Hignett, P., J. P. Taylor, and P. N. Francis, Comparison of observed and modeled direct aerosol forcing during TARFOX, *J. Geophys. Res.*, 104, 2279–2287, 1999.
- Hirst, E., P. H. Kaye, R. S. Greenaway, P. Field, and D. W. Johnson, Discrimination of micrometre-sized ice and supercooled droplets in mixed-phase cloud, *Atmos. Environ.*, 35, 33–47, 2001.
- Intergovernmental Panel on Climate Change (IPCC), *Climate Change 2001: The Scientific Basis, Contribution of Working Group I to the Third Assessment Report of the Intergovernmental Panel on Climate Change*, edited by J. T. Houghton et al., 881 pp., Cambridge Univ. Press, New York, 2001.
- Karyampudi, V. M., et al., Validation of the Saharan dust plume conceptual model using lidar, Meteosat, and ECMWF data, *Bull. Am. Meteorol. Soc.*, 80, 1045–1075, 1999.
- Kaufman, Y., D. Tanré, O. Dubovik, A. Karnieli, and L. A. Remer, Absorption of sunlight by dust as inferred from satellite and ground-based remote sensing, *Geophys. Res. Lett.*, 28, 1479–1483, 2001.
- Loeb, N. G., and S. Kato, Top-of-atmosphere direct radiative effect of aerosols over the Tropical Oceans from the Clouds and the Earth's Radiant Energy System (CERES) satellite instrument, *J. Clim.*, 15, 1474–1484, 2002.

- Myhre, G., and F. Stordal, Global sensitivity experiments of the radiative forcing due to mineral aerosols, *J. Geophys. Res.*, *106*, 18,193–18,204, 2001.
- Myhre, G., A. Grini, J.M. Haywood, F. Stordal, B. Chatenet, D. Tanré, J. Sundet, and I. Isaksen, Modeling the radiative impact of mineral dust during the Saharan Dust Experiment (SHADE) campaign, *J. Geophys. Res.*, *108*(D18), doi:10.1029/2002JD002566, in press, 2003.
- Nakajima, T., G. Tonna, R. Rao, Y. Kaufman, and B. Holben, Use of sky brightness measurements from ground for remote sensing of particulate polydispersions, *Appl. Opt.*, *35*, 2672–2686, 1996.
- Patterson, E. M., D. A. Gillitte, and B. H. Stockton, Complex index of refraction between 300 and 700 nm for Saharan aerosols, *J. Geophys. Res.*, *82*, 3153–3167, 1977.
- Ramaswamy, V., O. Boucher, J. Haigh, D. Hauglustaine, J. M. Haywood, G. Myhre, T. Nakajima, G. Y. Shi, and S. Solomon, Radiative forcing of climate change, in *Climate Change 2001: The Scientific Basis, Contribution of Working Group I to the Third Assessment Report of the Intergovernmental Panel on Climate Change*, edited by J. T. Houghton, pp. 349–416, Cambridge Univ. Press, New York, 2001.
- Smith, G. L., R. N. Green, E. Raschke, L. M. Avis, J. T. Suttles, B. A. Wielicki, and R. Davies, Inversion methods for satellite studies of the earth radiation budget: Development of algorithms for the ERBE mission, *Rev. Geophys.*, *24*, 407–421, 1986.
- Sokolik, I. N., and O. B. Toon, Direct radiative forcing by anthropogenic airborne mineral aerosols, *Nature*, *381*, 681–683, 1996.
- Sokolik, I. N., D. M. Winker, G. Bergametti, D. A. Gillette, G. Carmichael, Y. J. Kaufman, L. Gomes, L. Schuetz, and J. E. Penner, Introduction to special section: Outstanding problems in quantifying the radiative impacts of mineral dust, *J. Geophys. Res.*, *106*, 18,015–18,027, 2001.
- Tanré, D., et al., Measurement and modeling of the Saharan dust radiative impact: Overview of the Saharan Dust Experiment (SHADE), *J. Geophys. Res.*, *108*(D18), doi:10.1029/2002JD003273, in press, 2003.
- Tegen, I., and I. Fung, Contribution to the atmospheric mineral aerosol load from land surface modification, *J. Geophys. Res.*, *100*, 18,707–18,726, 1995.
- Thomas, G. E., and K. Stamnes, *Radiative Transfer in the Atmosphere and Ocean*, Cambridge Univ. Press, New York, 1999.
- Wielicki, B. A., B. R. Barkstrom, E. F. Harrison, R. B. Lee III, G. L. Smith, and J. E. Cooper, Clouds and the Earth's Radiant Energy System (CERES): An Earth observing system experiment, *Bull. Am. Meteorol. Soc.*, *77*, 853–868, 1996.
- Woodward, S., Modeling the atmospheric life-cycle and radiative impact of mineral dust in the Hadley Centre climate model, *J. Geophys. Res.*, *106*, 18,155–18,166, 2001.
- World Climate Program (WCP), A preliminary cloudless standard atmosphere for radiation computation, World Meteorol. Org., Geneva, 1986.
-
- P. Formenti, Laboratoire Interuniversitaire des Systèmes Atmosphériques (LISA), Faculté des Sciences et Technologie, 61 Avenue du Général de Gaulle, F-94010 Créteil, France. (formenti@lisa.univ-paris12.fr)
- P. N. Francis, M. D. Glew, J. M. Haywood, and S. R. Osborne, Met Office, Y46 Bldg, DERA, Farnborough, Hants GU14 0LX, UK. (jim.haywood@metoffice.com; pete.francis@metoffice.com; simon.osborne@metoffice.com; martin.glew@metoffice.com)
- E. J. Highwood, Met Department, Reading University, Reading, Berkshire, UK. (E.J.Highwood@met.rdg.ac.uk)
- E. Hirst, STRC, University of Hertfordshire, Hatfield, Herts AL10 9AB, UK. (E.Hirst@herts.ac.uk)
- N. G. Loeb, NASA Langley Research Center, 21 Langley Boulevard, Hampton, VA 23681-2199, USA. (n.g.loeb@larc.nasa.gov)
- G. Myhre, Department of Geophysics, University of Oslo, Blindern, Oslo, Norway. (gunnar.myhre@geofysikk.uio.no)
- D. Tanré, Laboratoire Optique Atmosphérique, Bat.P5, U.S.T. de Lille, Villeneuve d'Ascq, France. (tanré@loa.univ-lille1.fr)